Dynamics of Tpm1.8 domains on actin filaments with single-molecule resolution

Ilina Bareja[a,†], Hugo Wioland[b], Miro Janco[a], Philip R. Nicovich[a,‡], Antoine Jégou[b], Guillaume Romet-Lemonne[b], James Walsh[a,*], and Till Böcking[a,*]

[a]EMBL Australia Node in Single Molecule Science and ARC Centre of Excellence in Advanced Molecular Imaging, School of Medical Sciences, UNSW Sydney, Sydney, NSW 2052, Australia; [b]Université de Paris, CNRS, Institut Jacques Monod, 75006 Paris, France

ABSTRACT **Tropomyosins regulate the dynamics and functions of the actin cytoskeleton by forming long chains along the two strands of actin filaments that act as gatekeepers for the binding of other actin-binding proteins. The fundamental molecular interactions underlying the binding of tropomyosin to actin are still poorly understood. Using microfluidics and fluorescence microscopy, we observed the binding of the fluorescently labeled tropomyosin isoform Tpm1.8 to unlabeled actin filaments in real time. This approach, in conjunction with mathematical modeling, enabled us to quantify the nucleation, assembly, and disassembly kinetics of Tpm1.8 on single filaments and at the single-molecule level. Our analysis suggests that Tpm1.8 decorates the two strands of the actin filament independently. Nucleation of a growing tropomyosin domain proceeds with high probability as soon as the first Tpm1.8 molecule is stabilized by the addition of a second molecule, ultimately leading to full decoration of the actin filament. In addition, Tpm1.8 domains are asymmetrical, with enhanced dynamics at the edge oriented toward the barbed end of the actin filament. The complete description of Tpm1.8 kinetics on actin filaments presented here provides molecular insight into actin–tropomyosin filament formation and the role of tropomyosins in regulating actin filament dynamics.**

Monitoring Editor
Thomas Pollard
Yale University

Received: Oct 25, 2019
Revised: Aug 19, 2020
Accepted: Aug 21, 2020

INTRODUCTION

Actin is a highly conserved protein found in all eukaryotic cells. With the help of a myriad of actin-binding proteins (ABPs), actin filaments form extensive, highly dynamic networks that are associated with various structures and functions, including cell division, migration, intracellular transport, and cell–cell and cell–matrix adhesion (Pollard, 2016). Among the ABPs, tropomyosin is well known for its roles in the regulation and stabilization of actin filaments. There are multiple isoforms of tropomyosin (~40 in mammals), which are associated with functionally distinct populations of actin filaments (Gunning *et al.*, 2015). Tropomyosin is thought to facilitate functional specialization by controlling the recruitment of specific sets of actin-binding proteins in an isoform-specific manner (Tojkander *et al.*, 2011; Johnson *et al.*, 2014; Gunning *et al.*, 2015). Recent studies indicate that the majority of actin filaments in the cell are present as copolymers with tropomyosin (Meiring *et al.*, 2018). Thus, to properly understand the variable functions and dynamics of actin filaments, it becomes crucial to elucidate the fundamental molecular interactions between actin and tropomyosin.

Each tropomyosin molecule is a parallel dimeric alpha-helical coiled coil that covers six or seven actin monomers, depending on whether the isoform is low or high molecular weight (Khaitlina, 2015). Individual tropomyosin molecules bind very weakly to actin ($K_a \sim 3 \times 10^3\ M^{-1}$) (Wegner, 1980; Weigt *et al.*, 1991; Tobacman, 2008); however, tropomyosin is able to polymerize along actin,

This article was published online ahead of print in MBoC in Press (http://www.molbiolcell.org/cgi/doi/10.1091/mbc.E19-10-0586) on August 26, 2020.

Present address: [†]Department of Bionanoscience, Kavli Institute of Nanoscience Delft, Delft University of Technology, Van der Maasweg 9, 2629 HZ Delft, The Netherlands; [‡]Allen Institute for Brain Science, Seattle, WA 98109.

Author contributions: G.R.L., I.B., J.W., and T.B. conceptualized the project; A.J., G.R.L., I.B., J.W., and M.J. defined the methodology; J.W. provided the software; M.J. and P.R.N. provided resources; H.W. and I.B. investigated; H.W. validated the results; H.W., I.B., and J.W. performed formal analysis; I.B., J.W. and T.B wrote the original draft of the paper; all authors reviewed and edited the paper.

*Address correspondence to: James Walsh (james.walsh@phys.unsw.edu.au); Till Böcking (till.boecking@unsw.edu.au).

Abbreviations used: ABP, actin binding protein; ADP, adenosine diphosphate; ADP-F-actin, ADP bound actin polymer; PDMS, polydimethylsiloxane; TIRF, total internal reflection microscopy; Tpm1.8, tropomyosin isoform 1.8.

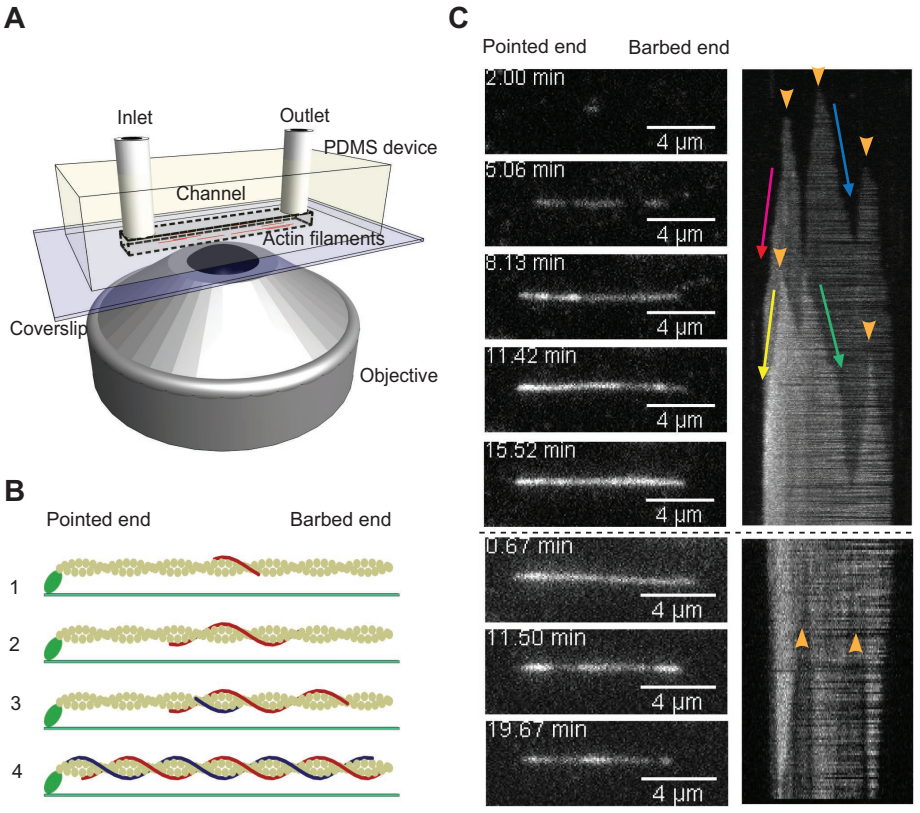

FIGURE 1: Real time observation of Tpm1.8 assembly and disassembly on actin filaments by TIRF microscopy. (A) Microfluidics and TIRF setup. (B) Schematic of the steps leading to decoration of an actin filament with tropomyosin: (1) A tropomyosin molecule (red) binds to a random site on one of the two strands on a naked actin filament attached to the surface via spectrin-actin seeds (green). (2) Domain elongation: tropomyosin molecules then bind at adjacent sites and form head-to-tail overlap complexes with the already bound tropomyosin molecule to extend the domain toward both the pointed and barbed ends of the actin filament. (3) Domain appearance and elongation occurs on both strands of the actin filament, as shown by a second (blue) tropomyosin strand. (4) Finally, the double helical actin filament is coated by two tropomyosin chains. The process of dissociation occurs by reversing the process, whereby tropomyosin can dissociate from either of the two ends of the tropomyosin strands located on both strands. (C) Kymographs and snapshots from a time-lapse series of a single actin filament showing Tpm1.8 association (top) and dissociation (bottom) after injection and wash-out of mNeonGreen-Tpm1.8, respectively. The two levels of fluorescence intensity correspond to Tpm1.8 domains on either one or both actin strands. Orange arrow heads: nucleation points during association and points where dissociation starts after mNeonGreen-Tpm1.8 wash-out. Arrows indicate the slopes used to measure the elongation rate toward either end.

which drastically strengthens its binding affinity through avidity (Wegner, 1979; Wegner, 1980; Singh and Hitchcock-DeGregori, 2009). Tropomyosin molecules bind to the two strands of the double-helical actin filament, where they interact in a head-to-tail manner to form two continuous chains that wrap around the actin filament (Perry, 2001; Li *et al.*, 2011; Khaitlina, 2015), as shown schematically in Figure 1B.

Cell-biological and biochemical techniques have been used extensively to identify different tropomyosin isoforms, their localization, and the corresponding ABPs they regulate (Bryce *et al.*, 2003; Creed *et al.*, 2011; Tojkander *et al.*, 2011; Brayford *et al.*, 2016; Gateva *et al.*, 2017; Pathan-Chhatbar *et al.*, 2017). Ensemble measurements (solution assays) have shown differences in the affinity and cooperativity of tropomyosin isoforms binding to actin and in their effect on actin assembly kinetics (Janco *et al.*, 2016). However, the self-assembly of tropomyosin on actin filaments is a highly stochastic and nonlinear process, which is difficult to resolve using ensemble measurements. Basic nucleation and growth models have been proposed (Vilfan, 2001) that are able to recapitulate observations from ensemble measurements (Wegner, 1979, 1980; Wegner and Walsh, 1981; Keiser and Wegner, 1985; Wegner and Ruhnau, 1988; Weigt *et al.*, 1991). Parameterization from these models suggests that binding of tropomyosin to actin filaments involves a slow initial nucleation step followed by rapid elongation.

Recent developments in reconstituting actin filaments near surfaces for observation by time-lapse fluorescence microscopy have enabled the study of various processes regulating actin dynamics at a molecular level (Carlier *et al.*, 2014; Jégou and Romet-Lemonne, 2016; Shekhar and Carlier, 2016), including the interplay between different tropomyosins and other ABPs (Hsiao *et al.*, 2015; Schmidt *et al.*, 2015; Sckolnick *et al.*, 2016; Christensen *et al.*, 2017; Jansen and Goode, 2019). These studies demonstrate the power of this approach for dissecting individual steps of tropomyosin domain nucleation, elongation, and shrinkage on actin filaments, which will enable testing and refining our models of these processes. It remains largely unknown to what extent tropomyosin assembly differs between species and between isoforms. A dissection of the common and isoform-specific mechanisms governing the interplay of tropomyosin with actin and their relationship to function, especially in the context of the numerous cytosolic isoforms that are spatially and temporally regulated in mammalian cells (Gunning *et al.*, 2005), will therefore require detailed studies of individual isoforms that are involved in different actin-mediated processes.

The human cytosolic low–molecular weight isoform Tpm1.8 is associated with stress fibers and lamellipodia, where it is involved in regulating the highly dynamic process of cell migration (Bryce *et al.*, 2003; Brayford *et al.*, 2016). It exhibits one of the strongest affinities for actin (Moraczewska *et al.*, 1999), but its assembly and turnover on actin and how these properties relate to the dynamics of Tpm1.8-containing cellular actin structures remain unresolved. In this study, we used microfluidics and total internal reflection fluorescence (TIRF) microscopy to measure the dynamic interactions of Tpm1.8 molecules with preformed actin filaments in vitro at the single-filament and the single-molecule levels. Our data provide a complete experimentally parameterized model of Tpm1.8 assembly and disassembly kinetics on actin, providing molecular insight into the interplay between the two polymer systems.

RESULTS

Microfluidics experiments allow direct observation of Tpm1.8 dynamics on individual actin filaments in real time

We used a combination of microfluidics and TIRF microscopy to characterize the fundamental molecular interactions underlying

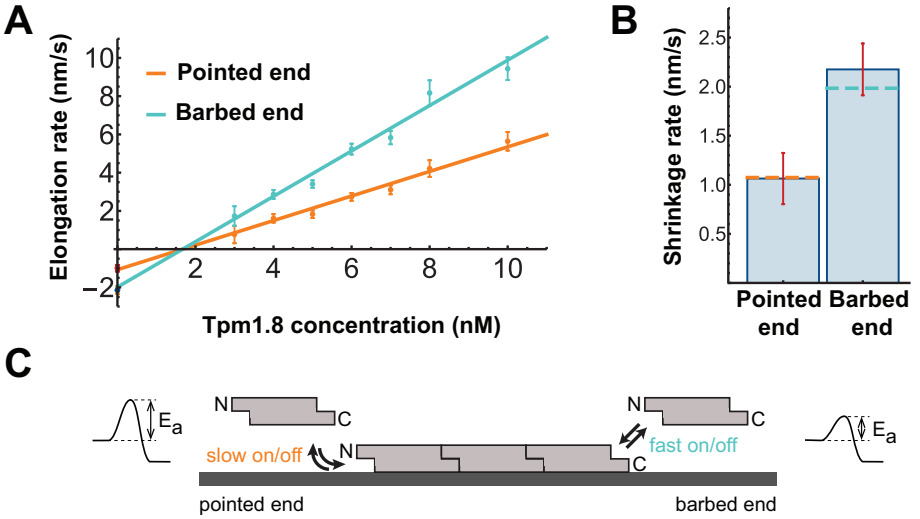

FIGURE 2: Tpm 1.8 domains grow and shrink faster at the domain edge directed towards the barbed end than the pointed end of the actin filament. (A) Tpm1.8 concentration dependence of domain elongation rates toward the barbed and pointed ends of the actin filament. The solid lines represent linear fits of the data, whereby the y-axis intercept of each fit line gives the shrinkage rate for the respective end, the x-axis intercept gives the critical concentration and the slope gives the elongation rate constant. Points represent the mean and error bars represent the standard deviation; N (number of filaments [slopes measured towards pointed/barbed end]) = 11 [2/13] (3 nM); 20 [35/66] (4 nM); 40 [73/116] (5 nM); 48 [109/121] (6 nM); 52 [99/110] (7 nM); 38 [73/90] (8 nM); 58 [148/178] (10 nM). (B) Comparison of shrinkage rates of Tpm1.8 at the two edges of a Tpm1.8 domain. The values for the shrinkage rates obtained from y-axis intercepts in (A) are represented by dotted lines. *N* (number of slopes) = 78 (pointed end), 111 (barbed end); $p = 6.6E\text{-}14$, unpaired Student's *t*-test, after Welch's correction. (C) Schematic of the binding of tropomyosin molecules to either end of an existing domain on an actin filament with corresponding potential energy diagrams of the reaction. N, N-terminal end; C, C-terminal end; Ea, activation energy.

tropomyosin binding to actin filaments, as shown in Figure 1A. We immobilized spectrin–actin seeds on the surface of a coverslip that formed the bottom of a microfluidic flow channel. The spectrin–actin seeds anchored actin filaments at their pointed ends and allowed the growth of actin filaments at the barbed ends. Each field of view typically contained 50–60 actin filaments (Supplemental Figure 1). After actin filaments were grown and aged to get ADP-F-actin, fluorescent Tpm1.8 was flowed into the channel and its binding to the actin filaments was directly imaged using TIRF microscopy. Throughout the acquisition, the filaments were kept aligned parallel to the surface by a constant flow of the solution. This approach allowed the proteins to bind freely to the filaments without any hindrance from the surface. After complete decoration of the filaments, the flow channel was washed with buffer and the dissociation of Tpm1.8 from the filaments was observed. We used recombinant Tpm1.8 fused at its N-terminus to an alanine–serine extension mimicking acetylation (Monteiro *et al.*, 1994) and to mNeonGreen.

Figure 1B summarizes the main steps of the actin–tropomyosin interaction that were characterized in this study. The initial assembly intermediates of new tropomyosin domains were detected as the appearance of diffraction-limited dots of fluorescent Tpm1.8 molecules. In the range of concentrations used, multiple such events were detected at different times and locations over the filaments; the number of observable stable domains per filament increased with concentration (Supplemental Figure 2). These dots then elongated in both directions until actin filaments (unlabeled) were fully decorated. The dissociation process, similarly, initiated at multiple points and at different times and the signal disappeared in both directions from the initiation points, which may in large part arise from gaps that remain between adjacent Tpm1.8 domains (Supplemental Figure 3). We were able to resolve the dynamics of Tpm1.8 domains on both strands of actin filaments, as seen by the two levels of fluorescence intensity in Figure 1C. Because Tpm1.8 binds tightly, complete dissociation was not observed at the time scales used for imaging, as seen from the kymograph. Combined, this system enabled us to observe the three basic steps of tropomyosin kinetics directly on both strands of actin filaments: the appearance of Tpm1.8 domains (nucleation), elongation as a result of binding of Tpm1.8 molecules to the edges of domains, and shrinkage as a result of dissociation of Tpm1.8 molecules from the edges of domains.

Tpm1.8 domains have asymmetric dynamics

The kymographs resulting from the microfluidic TIRF binding experiments were used to resolve the Tpm1.8 elongation and shrinkage kinetics toward both ends of the actin filament at a range of Tpm1.8 concentrations (Figure 2). The elongation rates were obtained from the kymographs by taking slopes that corresponded to the increase in fluorescence intensity with time, as illustrated in Figure 1C. As expected, the elongation rates increased linearly with concentration (Figure 2A). Surprisingly, the elongation toward the barbed end (1.19 $m{\cdot}M^{-1}{\cdot}s^{-1}$) was faster than that toward the pointed end (0.64 $m{\cdot}M^{-1}{\cdot}s^{-1}$) of the actin filament, with a ratio of 1.85 between these two rate constants. Similar elongation rates reflecting this asymmetry were measured when we reversed the polarity of actin filaments in the fluid flow by using gelsolin to anchor filaments to the surface from their barbed ends (Supplemental Table 1). We also compared the mNeonGreen–Tpm1.8 elongation kinetics on filaments grown from muscle actin (used throughout this work) and on filaments grown from cytoskeletal actin (which is the binding partner of Tpm1.8 in the cell) and found that the domain elongation rates toward both ends of the actin filament were essentially the same (Supplemental Figure 5). These observations showed that the asymmetry in elongation rates was independent of fluid flow or choice of actin isoform.

Fluorescence labeling of tropomyosins can impair their function, so that the effects of different labeling strategies depend on the isoform and experimental system. Fusion of a fluorescent protein tag to the N-terminus of Cdc8, the sole tropomyosin in fission yeast, does not perturb its assembly on actin filaments in vitro or localization in the cell (Brooker *et al.*, 2016) but leads to severe functional defects, in particular misregulation of actin nucleation and cell division (Wu *et al.*, 2003; Brooker *et al.*, 2016). These defects can be alleviated by using certain cysteine mutants of Cdc8, and Cdc8 labeled at the engineered cysteine can assemble on actin (Christensen *et al.*, 2017). N-terminal fusions of mammalian tropomyosins localize to the expected actin structures and support isoform-specific functions in cells (Tojkander *et al.*, 2011; Appaduray *et al.*, 2016;

Rate constant	Description	Parameter value (length)	Parameter value (molecules)	Source
B_I	Binding of an isolated Tpm to the actin filament	4.55×10^{11} $m^{-1}M^{-1}s^{-1}$ [a]	2.3×10^3 $M^{-1}s^{-1}$ [b]	Figure 5C
R_I	Release of an isolated Tpm from the actin filament	4.125×10^{-8} $m{\cdot}s^{-1}$ [c]	1.25 s^{-1}	Figure 4F
B_P	Binding to the domain edge at the pointed end	0.64 $m{\cdot}M^{-1}{\cdot}s^{-1}$ [d]	2×10^7 $M^{-1}{\cdot}s^{-1}$ [c]	Figure 2
B_B	Binding to the domain edge at the barbed end	1.19 $m{\cdot}M^{-1}{\cdot}s^{-1}$ [d]	3.6×10^7 $M^{-1}{\cdot}s^{-1}$ [c]	Figure 2
R_P	Release from the domain edge at the pointed end	1.07×10^{-9} $m{\cdot}s^{-1}$ [d]	0.033 s^{-1} [c]	Figure 2
R_B	Release from the domain edge at the barbed end	1.98×10^{-9} $m{\cdot}s^{-1}$ [d]	0.061 s^{-1} [c]	Figure 2
B_{BP}	Combined binding rate at both domain edges (B_B+B_P)	1.83 $m{\cdot}M^{-1}{\cdot}s^{-1}$ [d]	5.6×10^7 $M^{-1}{\cdot}s^{-1}$ [c]	Figure 2
R_{BP}	Combined release rate at both domain edges (R_B+R_P)	3.05×10^{-9} $m{\cdot}s^{-1}$ [d]	0.094 s^{-1} [c]	Figure 2

[a]Determined as a scaling factor in Figure 5C and expressed per unit length of actin filament.
[b]Calculated assuming that Tpm1.8 can bind to a naked actin filament at sites separated by an actin subunit (5 nm).
[c]Calculated assuming an effective length of 33 nm for the Tpm1.8 molecule.
[d]Obtained from Tpm1.8 domain length changes measured from kymographs.

TABLE 1: Summary of kinetic rate constants used for modeling.

Sao *et al.*, 2019); they also assemble on actin filaments in vitro (Gateva *et al.*, 2017). To test whether the N-terminal fluorescent protein affected the kinetics of Tpm1.8 in our assays, we monitored the assembly of an equimolar mixture of tagged and untagged Tpm1.8, which yielded elongation rates similar to those observed above (Supplemental Table 1). The fluorescence intensity of actin filaments decorated with the equimolar mixture was 42% of the value for fully tagged Tpm1.8, that is, close to the value expected for equal incorporation of tagged and untagged Tpm1.8. Furthermore, elongation kinetics of the related isoform Tpm1.1 fused to a fluorescent protein or labeled with an organic fluorophore on an internal cysteine were similar to each other, and assembly showed the same general features as for mNeonGreen–Tpm1.8, including the asymmetry in elongation rates (Supplemental Figure 4). Although it is likely that N-terminal fusions affect some function of tropomyosins, our observations suggest that the fluorescent protein tag had only a minor effect on elongation kinetics and actin affinity in our in vitro assays.

Domain shrinkage rates determined from the slopes of signal decrease in the kymographs after washout were independent of the mNeonGreen–Tpm1.8 concentration used to decorate the filaments before washout, as expected (Supplemental Figure 6). Domain shrinkage was also asymmetric (Figure 2B): Release of Tpm1.8 was 1.85 times faster from the domain edge directed toward the barbed end (1.98×10^{-9} $m{\cdot}s^{-1}$) than from that directed toward the pointed end (1.07×10^{-9} $m{\cdot}s^{-1}$) of the actin filament. Overall, our single-filament data reveal that the polarity of the actin filament with faster growth at the barbed end is reflected by the asymmetrical kinetics of Tpm1.8 domains with faster growth at the C-terminal edge (Figure 2C), with potential implications for allowing Tpm1.8 domain elongation to keep up with actin filament growth (Supplemental Figure 7).

To determine the effective length of a single Tpm1.8 molecule (i.e., the length added to a domain by addition of a Tpm1.8 molecule), we measured the fluorescence intensity per unit length of actin filaments fully decorated with mNeonGreen–Tpm1.8 (Supplemental Figure 8) and related this value to the fluorescence intensity of a single mNeonGreen–Tpm1.8 (Figure 4E, green curve). Using these values, we then found that each Tpm1.8 molecule covered a length of ~33 nm on an actin filament (Supplemental Figure 8), corresponding to six actin monomers (Holmes *et al.*, 1990; Dominguez and Holmes, 2011), as expected for low–molecular weight tropomyosin isoforms. The effective length can be used to convert the kinetic rates for association and dissociation determined from length changes in the fluorescence images into units of number of molecules per unit time (see Table 1).

Finally, we obtained estimates for the critical concentration for the elongation of Tpm1.8 (i.e., the concentration above which binding at domain edges occurs faster than dissociation) from the *x*-axis intercepts of the fit lines in Figure 2A. As the ratios between the elongation and shrinkage rates are the same for the two domain edges, the critical concentration is also the same toward the two ends of the actin filament (1.65 nM). As a result, there is no concentration where treadmilling (net growth at one domain edge and dissociation at the other) of Tpm1.8 occurs.

Tpm1.8 decorates the two actin filament strands independently

One unanswered question is whether tropomyosin domains on opposite actin strands can influence each other. We took advantage of our ability to distinguish Tpm1.8 domain kinetics on the two strands to address this question. We measured the following four rates from the corresponding slopes in the kymographs (Figure 1C): 1) first and 2) second level of increase in intensity at the barbed end of the domain (blue and green arrow, respectively) and 3) first and 4) second level of increase in intensity at the pointed end of the domain (red and yellow arrow, respectively). The concentration dependence of these elongation rates (Figure 3A) confirmed the asymmetry toward pointed and barbed ends noted above. However, no significant differences between the first and second strands were observed in the elongation rates in either direction (barbed or pointed). A corresponding analysis of dissociation rates showed that these were the same on stretches of actin filament coated with a Tpm1.8 domain on one or both strands of the actin filament (Figure 3B). Thus, there was no difference in the Tpm1.8 kinetics for the two strands of the actin filament, suggesting that binding of Tpm1.8 to the ends of existing domains occurs independently on each of the two actin strands.

Next, we asked whether the presence of a Tpm1.8 chain on one strand of the actin filament could enhance nucleation of a domain on the opposite strand of the actin filament, as observed for the fission yeast tropomyosin Cdc8 (Christensen *et al.*, 2017). To answer this question, we measured how frequently the second Tpm1.8 domain appeared opposite the first domain versus elsewhere on the actin filament. We also measured the length of the first domain (relative to the length of the actin filament) at the time of second domain appearance and determined the probability that the second

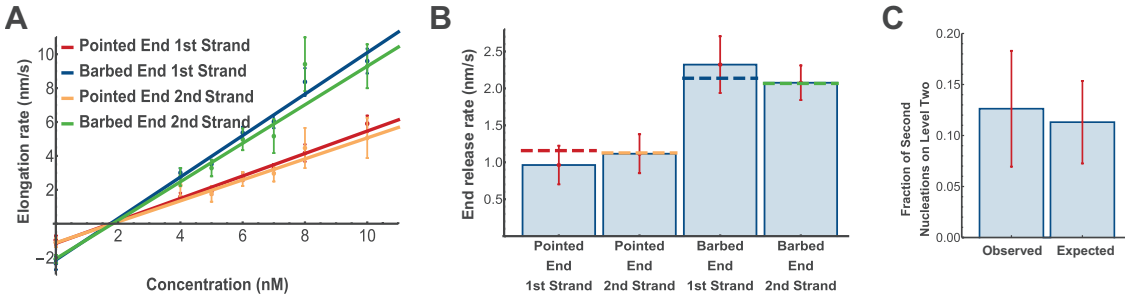

FIGURE 3: Tpm1.8 kinetics are unaffected by the presence of a Tpm1.8 domain on the opposite strand of the actin filament. (A) Plots of tropomyosin domain elongation kinetics toward the barbed and pointed ends of the actin filament as a function of Tpm1.8 concentration, with the data for both strands of the actin filament separated. The lines represent linear fits to the data. Data for pointed end/1st strand, *N* (number of slopes) = 25 (4 nM), 45 (5 nM), 63 (6 nM), 57 (7 nM), 46 (8 nM), 79 (10 nM); pointed end/2nd strand, *N* = 8 (4 nM), 16 (5 nM), 38 (6 nM), 35 (7 nM), 16 (8 nM), 49 (10 nM); barbed end/1st strand, *N* = 38 (4 nM), 71 (5 nM), 73 (6 nM), 72 (7 nM), 58 (8 nM), 89 (10 nM); barbed end/2nd strand, *N* = 18 (4 nM), 23 (5 nM), 32 (6 nM), 23 (7 nM), 15 (8 nM), 59 (10 nM). (B) Comparison of shrinkage kinetics of Tpm1.8 toward the two edges of a Tpm1.8 domain, with the data for both strands of the actin filament separated. The values for the dissociation rates obtained from y-axis intercepts in (A) are represented by dotted lines. *N* (number of slopes) = 16 (pointed end, 1st strand), 46 (pointed end, 2nd strand), 20 (barbed end, 1st strand), 82 (barbed end, 2nd strand); $p = 1.34E\text{-}12$ (pointed end versus barbed end) and $p = 0.89$ (1st strand versus 2nd strand) using two way ANOVA (Tukey test). (C) Frequency of the second Tpm1.8 domain nucleating opposite the already decorated region of the actin filament observed in 198 kymographs ("Observed"). To test for cooperativity of nucleation, this observed frequency of spatial coincidence is compared to the probability of spatial coincidence that is expected when the second domain nucleates at a random location in the undecorated region of the actin filament ("Expected"); one-tailed *t*-test ($p = 0.26$).

nucleation would occur opposite the first Tpm1.8 domain by chance (Figure 3C). We found that nucleations were observed opposite the first Tpm1.8 domain in 25 of 198 kymographs (12.6%), which was not significantly higher than expected by chance (11.3%), suggesting that Tpm1.8 domains have no or minimal effect on second strand nucleation. Overall, we conclude that there is no evidence for the existence of indirect binding cooperativity for Tpm1.8 domain nucleation or elongation between the two strands.

Tpm1.8 domains grow and shrink one tropomyosin molecule at a time

Using single-molecule imaging, we resolved the kinetics of newly formed Tpm1.8 domains on actin filaments to distinguish whether Tpm1.8 undergoes binding and dissociation as monomers or multimeric species. We immobilized actin filaments via multiple (nonspecific) anchoring points to the surface (Figure 4Ai). This immobilization method provided a greater number of filaments per field of view and also facilitated detection of single molecules because the filaments were static (in contrast to filaments grown from a spectrin–actin seed, which show movement at the nontethered end). We then flowed low concentrations of mNeonGreen–Tpm1.8 (3, 4, or 5 nM) over the actin to measure initial binding events (appearing as diffraction-limited spots) and early steps of domain elongation (Figure 4Aii), but not full decoration of actin filaments. Fluorescence intensity traces were generated at the sites of initial binding and analyzed with a step-fitting algorithm that could detect the increase or decrease of the fluorescence intensities as discrete quantal steps (Figure 4C).

We extracted the mNeonGreen–Tpm1.8 binding kinetics on surface-bound actin filaments by step fitting fluorescence traces recorded during the association phase. The distribution of dwell times between successive positive steps in the fluorescence intensity traces decayed exponentially (Supplemental Figure 9). The association rates obtained by fitting these exponentials for the respective concentrations are shown in Figure 4D and represent the addition of mNeonGreen–Tpm1.8 molecules at both edges of the Tpm1.8 domain. The polymerization rate constant estimated from this data (5.9×10^7 $M^{-1}{\cdot}s^{-1}$) was within 10% of the sum of the rate constants for growth at either end determined from the kymographs above (5.6×10^7 $M^{-1}{\cdot}s^{-1}$). We conclude that the kinetics observed at the filament scale (i.e., linear growth at the ends of domains) is consistent with the molecular scale for newly established domains.

To determine whether Tpm1.8 binds and dissociates from actin filaments solely as a monomer or higher-order species (dimer, trimers, etc.) are involved, we analyzed the step heights of the association and dissociation traces. To obtain a baseline for the fluorescence intensity of individual Tpm1.8 molecules, we sparsely immobilized Tpm1.8 on a coverslip and measured individual particle intensities. The intensity distributions for the first positive step (binding of the first Tpm1.8 molecule to a naked region of actin filament), for subsequent positive steps (association), and for negative steps (dissociation) are overlaid with the single-molecule intensity distribution of Tpm1.8 molecules in Figure 4E. The strong similarity between all four distributions suggests that Tpm1.8 binds, elongates, and dissociates from actin filaments as a monomer.

The observations above confirmed that the first assembly intermediate consists of an isolated (or solitary) Tpm1.8 bound to actin. This complex is thought to be highly unstable, but its half-life is unknown. To obtain insight into this process, we analyzed distributions of dwell times of fluorescence signals corresponding to single molecules bound to the filament at a given location and obtained a lower limit estimate for the dissociation rate of an isolated mNeonGreen–Tpm1.8 molecule of 1.25 s^{-1} (Figure 4F; see Supplemental Figure 10 for details).

Taken together, our observations suggest that all Tpm1.8 assembly and disassembly steps proceed in units of single molecules, so that the kinetics of binding and release from the ends of domains is independent of the length of the domains. Isolated tropomyosin molecules detach from the actin filaments at least an order of magnitude faster than from the edges of domains.

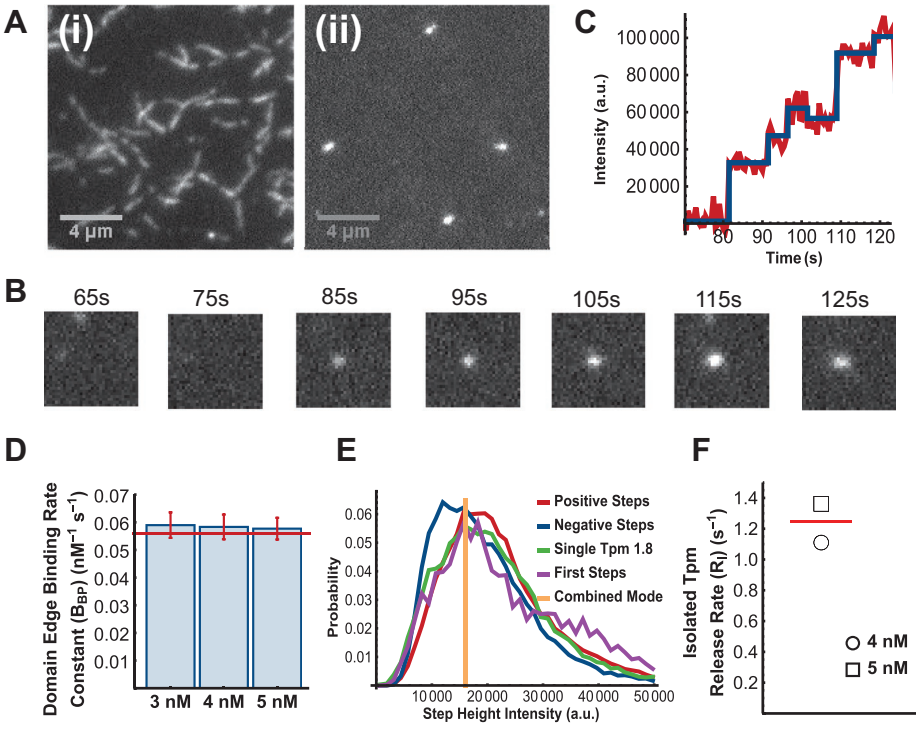

FIGURE 4: Single-molecule kinetics of Tpm1.8 on naked actin filaments and at the edges of diffraction-limited domains. (A) Assembly of mNeonGreen-Tpm1.8 on unlabelled actin filaments attached non-specifically to the surface. (i) TIRF image of actin filaments after complete decoration with mNeonGreen-Tpm1.8 (endpoint of the assembly process). (ii) TIRF image of actin filaments (unlabelled) with short mNeonGreen-Tpm1.8 domains that appeared shortly after injection of mNeonGreen-Tpm1.8 at a concentration of 3 nM. (B) Time-lapse images showing nucleation and growth of a diffraction-limited mNeonGreen-Tpm1.8 domain on an unlabelled actin filament. (C) Intensity trace of the mNeonGreen-Tpm1.8 segment shown in (B) recorded with an imaging frequency of 2 Hz with step fit (blue line) to identify times of addition/dissociation of Tpm1.8 molecules on the domain undergoing net elongation. (D) Combined rate constant for binding at both domain edges (R_{BP}) determined from step fitting of intensity traces of individual segments. The same rate constant determined from kymographs is shown for comparison. *N* (number of positive step times) = 13504 (3 nM), 15002 (4 nM), 14895 (5 nM). Errors represent the 95% CI of the residual of the fits (E) Distribution of mNeonGreen-Tpm1.8 intensity (green, determined by the intensity of molecules sparsely adhered to a clean glass surface) overlayed with intensity distributions of the first positive step (purple, binding of a mNeonGreen- Tpm1.8 molecule to a stretch of naked actin filament), all positive steps (red; binding events) and negative steps (blue; dissociation events) obtained from the step fitting of intensity traces of individual mNeonGreen-Tpm1.8 domains. *N* (number of events) = 12364 (single mNeonGreen-Tpm1.8 photobleaching), 4767 (first steps), 48168 (positive steps), 44641 (negative steps). (F) Estimated release rate (R_I) for an isolated mNeonGreen-Tpm1.8 molecule that binds to the actin filament (see Supplementary Figure 6 for details). N (number of single molecule events) = 9213 (4 nM), 15850 (5 nM).

A model of domain appearance with a stable nucleus containing only two Tpm1.8 molecules is sufficient to recapitulate experimental data

The early stages of tropomyosin domain formation on actin filaments have been difficult to establish. Studies have hinted at an initial slow process of nucleation followed by a faster process of elongation (Wegner and Ruhnau, 1988; Weigt *et al.*, 1991). However, it is still not known whether this "nucleus" consists of a minimum number of tropomyosins to be stable, and what the rate-limiting step of this reaction is. To address these questions, we compare experimental rates of domain appearance with theoretical predictions.

We obtained rates of domain appearance (nucleation events that proceed to form observable, elongating Tpm1.8 domains) by measuring the earliest time at which the first growing mNeonGreen–Tpm1.8 domain was detectable in the kymographs. For this analysis we considered only the appearance of the first domain for each filament, that is, when the entire filament was available for binding. We assumed that the probability of domain appearance per unit length per unit time is constant, that is, the time taken for the initial event should be inversely proportional to the length of the filament. Therefore, we multiplied the appearance time by the length of the filament and used this measure to generate survival curves of filaments that remain without Tpm1.8 domains. Exponential fits of these survival curves then provided experimental rates for domain appearance (Supplemental Figure 11), which increased nonlinearly with increasing Tpm1.8 concentration (Figure 5C, red data points).

The kinetic interactions observed in this work are summarized in Figure 6: reversible weak binding of the first tropomyosin molecule to an undecorated stretch of actin filament is followed by reversible addition of tropomyosin molecules to the edges of the growing domain. The domain appearance rate can be described as split into two components: 1) the binding of the first tropomyosin molecule (as a rate $c \cdot B_I$) and 2) the probability of continued growth into a tropomyosin strand, that is, success of nucleation. Together, the domain appearance rate (k_{DA}) can be expressed as

$$k_{DA} = c \cdot B_I \cdot S(c)$$

where c is the tropomyosin concentration, B_I is the on-rate constant of an isolated tropomyosin molecule binding to the actin filament, and $S(c)$ is the probability of continued growth into an observable tropomyosin domain, that is, successful nucleation.

To explore the interplay between the set of kinetic interactions described in Figure 6 and the probability of continued growth into an observable tropomyosin domain, we converted these interactions into a state space model where each state was denoted by the length of the tropomyosin domain and transitions between states are governed by the effective experimentally measured rates (see the Supplemental Information for details). Using this model, we calculated the probability of continued growth, $S(c)$, by multiplying all of the transition probabilities from the single tropomyosin state to an infinitely long domain, which gives

$$S(c) = \frac{cB_{BP} - R_{BP}}{R_I + cB_{BP} - R_{BP}}$$

where c is the tropomyosin concentration, B_{BP} and R_{BP} are the sums of binding and release rate constants, respectively, for the

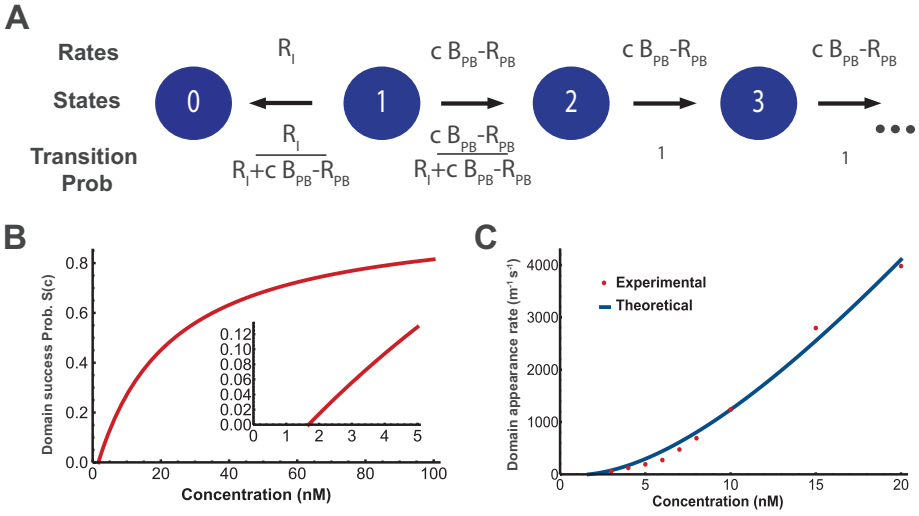

FIGURE 5: Analysis of domain appearance. (A) A simplified model of the growth pathway for a newly formed domain. Single (isolated) Tpm molecules bound to actin are in state 1. Single molecules that dissociate move to the 0 state at the release rate, RI. Alternatively, a second molecule may bind to the isolated Tpm (1), moving it to state 2. Addition of Tpm to states containing one or more molecules is governed by the elongation rate ($c{\cdot}B_{BP}{-}R_{PB}$, where c is the Tpm concentration, B_{BP} and R_{PB} are the rate constants for binding and release at both edges of the domain). The probability of each reaction is given by dividing each rate by the sum of the rates of reactions out of the relevant state. (B) Plot of the probability of domain appearance as a function of concentration calculated using the model in (A). The inset shows the low concentration regime of the curve. (C) Domain appearance rate measured experimentally (red dots) from single filaments kymographs (Supplementary Figure 7), and fitted with the nucleation model (blue curve) with the rate constant (BI) for binding of an isolated Tpm to the naked actin filament as the only free parameter, yielding a value of BI = 455 $nm^{-1}\,M^{-1}\,s^{-1}$.

edges of the tropomyosin domain (measured experimentally in Figure 2; see Table 1), and R_I is the rate constant for release of an isolated tropomyosin molecule from the actin filament (measured experimentally in Figure 4; see Table 1). The plot of this function using the experimentally determined parameters (Figure 5B) shows that the probability of an observable domain appearing (i.e., leading to the growth of a Tpm1.8 domain) is zero at tropomyosin concentrations below the critical concentration for tropomyosin domain elongation, and then increases to asymptotically approach 1 at high concentrations; that is, at high concentrations, nucleation is controlled by the binding rate of an isolated tropomyosin molecule ($c \cdot B_I$). This calculation shows that in the regime that was probed experimentally (≤20 nM), the nucleation success probability was less than 45%. Figure 5C shows the fit of the nucleation model to the experimental data, in which B_I is the only free parameter used to minimize the least-squares difference with the experimental values, providing an estimate of B_I = 455 $nm^{-1}{\cdot}M^{-1}{\cdot}s^{-1}$ (see Supplemental Text and Supplemental Figures 12 and 13 for an alternative method of deriving a value for B_I/R_I from the experimental domain appearance rates).

The domain appearance model is able to reproduce the nonlinear increase in the nucleation rate with tropomyosin concentration, suggesting that the nucleation process is essentially governed by two sets of reaction rates for 1) binding/dissociation of the first tropomyosin to an undecorated section of an actin filament and 2) binding/dissociation of a tropomyosin molecule at the edges of a domain. We note that in this model the smallest domain at which the latter reaction rates become independent of domain length consists of only two tropomyosin molecules.

A limited set of kinetic parameters account for Tpm1.8 domain dynamics

To test whether the experimentally measured parameters are sufficient to reproduce all features of the observed tropomyosin kinetics, we combined the interactions investigated here (summarized in Figure 6A) into an experimentally parameterized stochastic model (see Table 1 for parameter values and the measurements from which they were derived). In this model, we assumed that independently nucleated tropomyosin domains anneal into a single chain when they have sufficiently elongated toward each other to form a contact. In reality, domains presumably only end up annealing into a single chain when they are in register with each other; that is, the gap between the two domains is a multiple of the length of the Tpm1.8 binding site (six actin subunits; Supplemental Figure 3). However, given how tightly Tpm1.8 binds, this simplification does not have a significant effect on the kinetics of filament decoration. The kymographs generated using the model at a range of Tpm1.8 concentrations resembled the experimental kymographs (Figure 6B) and faithfully reproduced elongation kinetics and domain appearance rates (Supplemental Figure 14). Overall, this comparison confirmed that the steps incorporated into our model were sufficient to predict the experimental kinetics of Tpm1.8 assembly.

DISCUSSION

Direct observation of Tpm1.8 assembly on actin filaments in vitro at the single-molecule and single-filament levels with unparalleled resolution enabled us to measure the assembly units and kinetics of Tpm1.8 domain appearance, elongation, and shrinkage. On the basis of our observations we propose the following pathway: all association/dissociation steps occur in units of single (dimeric) tropomyosin molecules. A tropomyosin molecule in solution binds to actin with low affinity. Unless additional molecules bind to the first isolated molecule to form a stable domain on actin, it rapidly dissociates into solution. Binding and release occur at both edges of the tropomyosin domain, but more rapidly at the domain edge oriented toward the barbed than toward the pointed end of the actin filament. Overall domain elongation rates are the same for diffraction-limited (<10 molecules) and microscopic (10 to >100 molecules) domains; there is no apparent dependence of elongation on domain length. A stochastic model incorporating these reactions is sufficient to simulate experimentally observed tropomyosin kinetics, including rates of domain appearance, suggesting that there are no additional steps governing this process.

The complex between an isolated Tpm1.8 molecule and the actin filament is short-lived (half-life of ~0.6 s or less) and has a low affinity ($K_d = R_I/B_I \approx 500$ μM), while a tropomyosin molecule bound at the edge of a domain has a longer half-life (11 s and 21 s at the barbed and pointed ends, respectively) and a profoundly higher affinity (given by the critical concentration of 1.65 nM). Our analysis

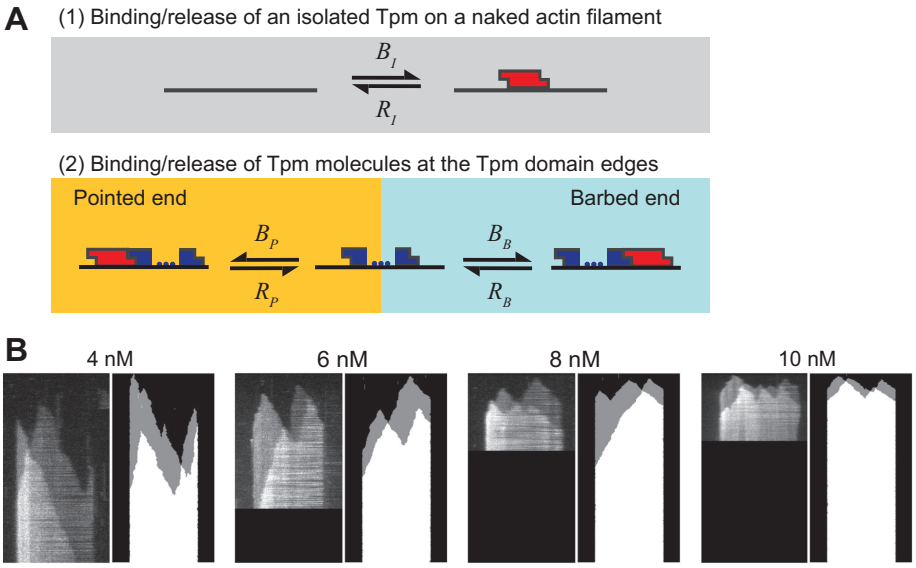

FIGURE 6: Simulated kymographs of Tpm1.8 assembly on actin filaments obtained with a kinetic model reproduce the features of kymographs from experiments. (A) Schematic representation of the model for tropomyosin kinetics on actin filaments. All binding (and dissociation) processes occur by the addition of single Tpm1.8 molecules (shown in red). (B) Comparison of experimental and simulated kymographs at a range of Tpm1.8 concentrations. The lengths of filaments from the experiment are 8.449, 8.608, 9.591 and 9.619 μm for 4, 6, 8 and 10 nM Tpm1.8, respectively. The time of acquisition is 55.84, 39.87, 23.34 and 20 min for 4, 6, 8 and 10 nM Tpm1.8, respectively. The simulated kymographs are 8 μm in length. Kymographs are representative of the types of kymographs randomly generated by the simulation.

suggests that this pronounced increase in stability is largely achieved upon binding of a second tropomyosin to the first (solitary) molecule on actin. That is, we propose that the minimal domain (or nucleus) with sufficient stability so that it can grow or shrink with approximately the same kinetics as much longer domains consists of just two molecules. This model is supported by the single-molecule data, where dissociation of domains with two or more tropomyosin molecules was not prominent. Indeed, a domain consisting of two Tpm1.8 molecules almost wraps around the actin filament, and it is tempting to speculate that shorter tropomyosins (such as those found in yeast) would require three molecules to form a stable domain. Nucleation occurs at all tropomyosin concentrations above the critical concentration (1.65 nM) and ultimately leads to the complete decoration of the actin filament (as long as tropomyosin is in excess of actin), consistent with the cooperativity of tropomyosin assembly on actin (Wegner, 1979). However, at low concentrations this process is slow because most isolated tropomyosins binding to a naked actin filament fall off before they are stabilized by a second molecule to form a growing domain (Figure 4B). Tuning the affinity of an isolated tropomyosin for actin provides a potential control mechanism, in which increasing the affinity would accelerate domain appearance (nucleation), while a decrease would make nucleation so improbable that it would not occur on relevant timescales.

Tropomyosin cooperativity due to the overlap between N- and C-termini of adjacent molecules in the chain is considered an important characteristic of F-actin network formation, organization, and ABP sorting (Gunning *et al.* 2015). In addition, it has been proposed that long-range binding cooperativity may arise from the interaction between the two tropomyosin chains binding to the two strands of the actin filament (Schmidt *et al.* 2015; Christensen *et al.* 2017). Thus, the presence of a tropomyosin chain on one strand of the actin filament may enhance binding of tropomyosin on the opposite strand, which could result in enhanced domain nucleation and/or elongation. We tested for the existence of this additional cooperativity in our data by comparing the elongation and shrinkage rates for the two tropomyosin chains, represented by the two levels of fluorescence intensity in the kymographs. From these measurements, we observed no difference in the kinetics for the two Tpm1.8 chains. We also observed no increase in domain nucleation frequency opposite of an existing Tpm1.8 strand. Taken together our observations indicate that Tpm1.8 binds independently on the two strands of actin filaments (Figure 3).

While the binding affinity of Tpm1.8 is the same at both edges of a domain, we discovered that the on-/off-kinetics are up to twofold faster at one edge than at the other, as previously observed (albeit to a lesser extent) for the yeast tropomyosin Cdc8 (Christensen *et al.* 2017). Tropomyosin chains are oriented on the actin filament so that N-terminus of tropomyosin is directed toward the pointed end while the C-terminus is directed toward the barbed end (Orzechowski *et al.* 2014; Figure 2C). The asymmetry in rates at opposing edges could result from an increased activation energy barrier for binding and dissociation at the domain edge with exposed N-terminus as compared with the domain edge with exposed C-terminus (Figure 2C). Such an increase in activation energy could arise if the N-terminus of a tropomyosin bound to actin were poorly accessible, for example, due to reduced conformational plasticity required for forming an overlap junction (Orzechowski *et al.* 2014). It should be noted that the N-terminal fluorescent protein tag used here can affect the molecular interactions between tropomyosins and between tropomyosin and actin, but the principal characteristics of mNeonGreen–Tpm1.8 kinetics, including asymmetry, were also observed for mixtures of tagged and untagged Tpm1.8 as well as for Tpm1.1 labeled with an organic fluorophore at the cysteine residue at position 190. The physiological relevance of the asymmetry in kinetics at opposing domain edges, if present for native tropomyosins in the cell, is unclear, but may be relevant for a potential role of Tpm1.8 in regulating actin dynamics (for example, in lamellipodia, Brayford *et al.* 2016) or its interplay with other actin-binding proteins.

Several features of mNeonGreen–Tpm1.8 assembly have been observed before with chemically labeled tropomyosin isoforms from a range of species. Nucleation of multiple domains on both strands of the actin filament as well as bidirectional domain growth leading to full decoration have been observed for mammalian Tpm1.1 produced recombinantly (Nicovich *et al.* 2016; Janco *et al.* 2018) or purified along with other isoforms from muscle (Schmidt *et al.* 2015). These features have also been observed for fission yeast Cdc8 (Christensen *et al.* 2017; Palani *et al.* 2019) and nonmuscle *Drosophila* Tm1A (Hsiao *et al.* 2015). Interestingly, Tm1A preferentially nucleates domains on ADP-bound regions of the actin filament near the pointed end, which then elongate toward the pointed end (Hsiao *et al.* 2015). Other characteristics either have not been measured for other isoforms or show different behavior, such as binding

cooperativity for tropomyosin domain nucleation on opposite strands on the actin filament (absent for Tpm1.8 but observed for Cdc8; Christensen *et al.* 2017).

In this work, we have characterized the molecular interactions of Tpm1.8 binding to actin. This provides a platform for unraveling how tropomyosin decoration of actin is controlled within human cells. Similar approaches can be applied to other isoforms of tropomyosin to further identify characteristics common to isoforms associated with similar functions. Further, the addition of regulatory proteins or drugs will allow identification of the specific molecular interaction being affected.

MATERIALS AND METHODS

Constructs

The coding sequence for a fusion protein of mNeonGreen and mRubyII Tpm1.8 was cloned into a pET28a(+) vector using the *Eco*RI and *Xho*I sites, and additional features were introduced using site-directed mutagenesis. Expression of the final construct yields a protein (referred to as mNeonGreen–Tpm1.8 and mRubyII–Tpm1.8) with an N-terminal His_6-tag followed by mNeonGreen and a peptide linker (GGGSGGGSGTAS) fused to the N-terminus of Tpm1.8. The coding sequence for a fusion protein of mCherry and Tpm1.8 was cloned into a pHAT vector using the *Bgl*II and *Hind*III sites. Expression of the final construct yields a protein (referred to as mCherry–Tpm1.8) with an N-terminal His_6-tag followed by mCherry and a peptide linker (SGLRSGGGGSGGGGSGTAS) fused to the N-terminus of Tpm1.8.

Protein expression and purification

The fusion proteins mNeonGreen–Tpm1.8 and mRubyII–Tpm1.8 were expressed in Rosetta pLysS cells grown in 1 L of LB broth containing 50 µg/ml kanamycin at 37°C. The fusion protein mCherry–Tpm1.8 was expressed in BL21 DE3 star cells grown in 1 L of LB broth containing 0.1 mg/ml ampicillin at 37°C. Protein expression was induced with IPTG (1 mM) when the $O.D_{600}$ reached 0.6 and the cells were grown for an additional 4 h. Cells were pelleted by centrifugation (F10S-6 × 500Y rotor, Sorvall RC6) at 8000 rpm for 10 min at 4°C. The cell pellet was stored at −40°C until use. The pellet was resuspended in lysis buffer (20 mM Tris-HCl pH 7.8, 500 mM NaCl, 1 mM NaN_3, 5 mM imidazole, 2 mM $MgCl_2$, 0.1% Triton X100, 2% glycerol, 1 mM phenylmethylsulfonyl fluoride [PMSF], and a Roche–Hitachi EDTA free protease inhibitor tablet) and sonicated (8 min, 15 s on, 15 s off). The lysate was centrifuged (R18A rotor, Hitachi VX22N) at 15,000 rpm for 60 min at 4°C. The supernatant was filtered using a 0.45-µm syringe filter and loaded onto a 5-ml Hi-Trap column (GE Healthcare Life Sciences) equilibrated with lysis buffer. The column was washed with 50 mL buffer containing 30 mM imidazole, 500 mM NaCl, 20 mM Tris, 2 mM $MgCl_2$, 1 mM NaN_3 at pH 7.8 followed by 75 mL buffer containing 100 mM imidazole. The protein was eluted using a buffer containing 250 mM imidazole. The fractions with the protein were pooled and further purified by size exclusion chromatography using a 16/60 superdex 75pg column (GE Healthcare Life Sciences) equilibrated with a buffer containing 10 mM Tris pH 7.8, 150 mM NaCl, 1 mM EDTA, 2 mM DTT, 1 mM NaN_3, and 1% sucrose. The fractions containing protein were pooled, snap frozen in aliquots using liquid nitrogen, and stored at −80°C.

Microfluidics setup

Microfluidic devices with five channels (11 × 0.8 × 0.06 mm, L × W × H) were prepared from polydimethylsiloxane (PDMS) by replica molding and ports for tubing (inlet/outlet) were punched at the channel ends using a biopsy punch (diameter 0.7 mm). The device was washed with isopropanol and MilliQ water before use. Coverslips (Marienfeld superior No. 1.5H, 24 × 60 mm) were sonicated in filtered 100% ethanol for 30 min, washed with MilliQ water, sonicated in filtered 1 M NaOH for 30 min, and washed again with MilliQ water. The coverslips were blown dry under a stream of filtered nitrogen and then further dried at 70°C. The PDMS replica and the coverslip were treated with an air plasma for 3 min at 700 Torr. The channel device was assembled by pressing the PDMS replica onto the coverslip and annealing the device at 70°C for 4–5 h.

TIRF microscope setup

TIRF data were acquired using a custom-built TIRF microscope based around an ASI-RAMM frame (Applied Scientific Instrumentation) with a Nikon 100× CFI Apochromat TIRF (1.49 NA) oil immersion objective. Lasers were incorporated using the NicoLase system (Nicovich *et al.* 2017). Images were captured on two Andor iXon 888 EMCCD cameras (Andor Technology Ltd) and 300-mm tube lenses were used to give a field of view of 88.68 × 88.68 µm at Nyquist sampling frequency (86 nm per pixel). On our system we typically use a power density of ~1–3 W cm^{-2} (measured at the objective with the laser beam normal to the surface of the coverslip)

Channel preparation and surface chemistry for single-filament experiments

Anchoring of filaments at the pointed end using spectrin–actin seeds. Spectrin–actin seeds were prepared as described previously (Casella *et al.*, 1986), diluted in phosphate-buffered saline (PBS) to a final spectrin–actin concentration of 30 nM, injected into the channel, and allowed to incubate for 4 min. The channel was washed with PBS and incubated with a solution of PLL-PEG (SuSoS AG) in PBS (1 mg/ml) for 30–60 min. The channel was connected to the syringe pump via the outlet tubing and washed with Buffer F (5 mM Tris-HCl pH 7.8, 100 mM KCl, 0.2 mM ATP, 1 mM DABCO, 0.1 mM $CaCl_2$, 0.1% NaN_3, 10 mM DTT, 1 mg/ml bovine serum albumin [BSA], 1 mM $MgCl_2$, 0.2 mM EGTA). The channel was then filled with a BSA solution (10 mg/ml in PBS) and incubated for 5 min, followed by a wash with buffer F (0.8 µM, rabbit skeletal muscle actin, Hypermol E.K., Germany). A solution of G-actin in buffer F was flowed into the channel and actin filaments were grown from the surface-immobilized spectrin–actin seeds for 6 min. Actin was then flowed through the channel at its critical concentration (0.1 µM) for 15 min to prevent further polymerization or depolymerization and allow complete phosphate release.

Anchoring of filaments at the barbed end using gelsolin. Chambers were prepared as described above with the following modifications. The glass surface was passivated using PLL-PEG-biotin (1 mg/ml, >1 h). The surface was further passivated with BSA (5%, 10 min) and casein (Hammarsten Bovine, 5 mg/ml, 10 min). Neutravidin was injected (5 µg/ml, 10 min), followed by biotin–gelsolin (5 nM, 3 min, purified as described in Wioland *et al.* 2017). Unlabeled F-actin was prepolymerized (8 µM, > 1h), diluted to 0.8 µM, and injected in the microfluidic chamber to bind to surface-immobilized gelsolin.

Single-filament imaging of Tpm1.8 association and dissociation

A solution of mNeonGreen–Tpm1.8 in Buffer F (containing 0.1 µM actin to avoid depolymerization of actin filaments) was flowed through the channel at 30 µl/min and association on actin filaments attached to the glass surface was recorded by time-lapse TIRF imaging (488-nm laser, 20 mW, 30 ms exposure time) with a frame rate depending on the concentration of mNeonGreen–Tpm1.8. Dissociation was initiated by flowing Buffer F (containing 0.1 µM

actin) through the flow channel while recording TIRF images with a frame rate of 0.1 Hz.

Channel preparation and surface chemistry for single-molecule experiments

The channel was incubated with a solution of PLL-PEG (1 mg/ml in PBS) for 20 min, connected to the syringe pump via the outlet tubing, and washed with buffer F. A solution of 0.8 µM actin in Buffer F was flowed into the channel and incubated for 2 min. During this period, actin filaments polymerized in solution and adhered nonspecifically to the surface of the coverslip. A wash with Buffer F containing 0.1 µM actin was then given.

Single-molecule imaging of Tpm1.8 association and dissociation

A solution of mNeonGreen–Tpm1.8 (3, 4, or 5 nM) in Buffer F (containing 0.1 µM actin) was flowed through the channel and association on actin filaments attached to the glass surface was recorded by time-lapse TIRF imaging (488-nm laser, 45 mW, 50 ms exposure time). The length and frame rate of the acquisition were adjusted depending on the concentration to obtain a sufficient number of nucleation and elongation steps without significant photobleaching.

Image analysis at the level of single filaments

Elongation and dissociation rates. Kymographs of Tpm1.8 association and dissociation were generated using the FIJI kymograph plugin. The slopes of the kymographs were fitted using linear regression in Wolfram Mathematica to obtain elongation and dissociation rates. To determine the initial domain appearance rate, we assumed that the probability of binding anywhere on the filament is the same such that the time taken for the first nucleation to occur is inversely proportional to the length of the filament. Hence, the product of the time of the first nucleation event (t) and the length of the filament (l) is a constant. We plotted survival curves for the number of actin filaments without a nucleation event as a function of the $l \times t$ constant, which decreased exponentially. Fitting these exponentials gave the nucleation half-lives for different concentrations of Tpm1.8.

Nucleation cooperativity analysis

The experimental frequency of a second-domain nucleation occurring opposite the first domain was determined from kymographs. For each kymograph, we also measured the fraction (f) of the filament covered (on one strand) by the first Tpm1.8 domain at the nucleation time of the second domain. The probability that the second nucleation would occur opposite the first domain is then given by $f/(2 - f)$. The probability was further corrected for a slight bias in our data in detecting nucleation sites closer to the anchor site (possibly arising from actin filament dynamics and/or anchoring artefacts). Without this bias correction, the probability of spatial coincidence is 0.106 ± 0.02 (mean ± SD) for nucleation at random locations, which is not significantly lower than the experimental frequency ($p = 0.16$).

Image analysis at the single-molecule level

Image stacks were analyzed using the JIM Immobilized Microscopy Suite to extract intensity traces at sites corresponding to nucleation events (https://github.com/lilbutsa/JIM-Immobilized-Microscopy-Suite). Intensity traces were divided by the intensity of a dimeric mNeonGreen–Tpm1.8 molecule (equal to twice the intensity measured for mNeonGreen). Step fitting of traces was achieved using the findchangepts function in Matlab with a threshold of 0.03. Histograms of the intensity step heights for nucleation (first step), elongation (subsequent positive steps), and dissociation (negative steps) of Tpm1.8 were generated using Wolfram *Mathematica*. Cumulative probability functions of the time before a positive/negative step were fitted with single-exponential decays to obtain elongation/dissociation rates, respectively. Dividing the association rates by the concentration gave the association rate constant.

Stochastic Model

The stochastic model was solved using a custom program written in *Mathematica* 10.2 (Wolfram). The script used the Gillespie algorithm to generate statistically correct trajectories (Gillespie, 1976, 1977). A list containing the ends of each tropomyosin domain was used to calculate the probability of each reaction. The code for this program is freely available at (https://github.com/lilbutsa/Tropomyosin_Stochastic_Model).

ACKNOWLEDGMENTS

Funding (T.B.) came from from the Australian Research Council and National Health and Medical Research Council of Australia. Funding (A.J.) came from the European Research Council (grant StG-679116) We thank Peter Gunning for reagents and discussions and Richard Morris for discussions. We thank Bérengère Guichard for help with protein purification and molecular biology.

REFERENCES

Appaduray MA, Masedunskas A, Bryce NS, Lucas CA, Warren SC, Timpson P, Stear JH, Gunning PW, Hardeman EC (2016). Recruitment kinetics of tropomyosin Tpm3.1 to actin filament bundles in the cytoskeleton is independent of actin filament kinetics. PLoS One 11, e0168203.

Brayford S, Bryce NS, Schevzov G, Haynes EM, Bear JE, Hardeman EC, Gunning PW (2016). Tropomyosin promotes lamellipodial persistence by collaborating with Arp2/3 at the leading edge. Curr Biol 26, 1312–1318.

Brooker HR, Geeves MA, Mulvihill DP (2016). Analysis of biophysical and functional consequences of tropomyosin-fluorescent protein fusions. FEBS Lett 590, 3111–3121.

Bryce NS, Schevzov G, Ferguson V, Percival JM, Lin JJ-C, Matsumura F, Bamburg JR, Jeffrey PL, Hardeman EC, Gunning P, Weinberger RP (2003). Specification of actin filament function and molecular composition by tropomyosin isoforms. Mol Biol Cell 14, 1002–1016.

Carlier M-F, Romet-Lemonne G, Jégou A (2014). Actin filament dynamics using microfluidics. Methods Enzymol 540. 3–17.

Casella JF, Maack DJ, Lin S (1986). Purification and initial characterization of a protein from skeletal muscle that caps the barbed ends of actin filaments. J Biol Chem 261, 10,915–10,921.

Christensen JR, Hocky GM, Homa KE, Morganthaler AN, Hitchcock-DeGregori SE, Voth GA, Kovar DR (2017). Competition between tropomyosin, fimbrin, and ADF/Cofilin drives their sorting to distinct actin filament networks. eLife 6(March). https://doi.org/10.7554/eLife.23152.

Creed SJ, Desouza M, Bamburg JR, Gunning P, Stehn J (2011). Tropomyosin isoform 3 promotes the formation of filopodia by regulating the recruitment of actin-binding proteins to actin filaments. Exp Cell Res 317, 249–261.

Dominguez R, Holmes KC (2011). Actin structure and function. Annu Rev Biophys https://doi.org/10.1146/annurev-biophys-042910-155359.

Gateva G, Kremneva E, Reindl T, Kotila T, Kogan K, Gressin L, Gunning PW, Manstein DJ, Michelot A, Lappalainen P (2017). Tropomyosin isoforms specify functionally distinct actin filament populations in vitro. Curr Biol 27, 705–713.

Gillespie DT (1976). A general method for numerically simulating the stochastic time evolution of coupled chemical reactions. J Comput Phys https://doi.org/10.1016/0021-9991(76)90041-3.

Gillespie DT (1977). Exact stochastic simulation of coupled chemical reactions. J Phys Chem https://doi.org/10.1021/j100540a008.

Gunning PW, Hardeman EC, Lappalainen P, Mulvihill DP (2015). Tropomyosin—master regulator of actin filament function in the cytoskeleton. J Cell Sci 128, 2965–2974.

Gunning PW, Schevzov G, Kee AJ, Hardeman EC (2005). Tropomyosin isoforms: divining rods for actin cytoskeleton function. Trends Cell Biol 15, 333–341.

Holmes KC, Popp D, Gebhard W, Kabsch W (1990). Atomic model of the actin filament. Nature https://doi.org/10.1038/347044a0.
Hsiao JY, Goins LM, Petek NA, Mullins RD (2015). Arp2/3 complex and cofilin modulate binding of tropomyosin to branched actin networks. Curr Biol 25, 1573–1582.
Janco M, Böcking T, He S, Coster ACF, (2018). Interactions of Tropomyosin Tpm1.1 on a Single Actin Filament: A Method for Extraction and Processing of High Resolution TIRF Microscopy Data. PloS One 13, e0208586.
Janco M, Bonello TT, Byun A, Coster ACF, Lebhar H, Dedova I, Gunning PW, Böcking T (2016). The impact of tropomyosins on actin filament assembly is isoform specific. Bioarchitecture 6, 61–75.
Jansen S, Goode BL (2019). Tropomyosin isoforms differentially tune actin filament length and disassembly. Mol Biol Cell January, mbcE18120815.
Jégou A, Romet-Lemonne G (2016). Single filaments to reveal the multiple flavors of actin. Biophys J 110, 2138–2146.
Johnson M, East DA, Mulvihill DP (2014). Formins determine the functional properties of actin filaments in yeast. Curr Biol 24, 1525–1530.
Keiser T, Wegner A (1985). Isolation from bovine brain of tropomyosins that bind to actin filaments with different affinities. FEBS Lett 187, 76–80.
Khaitlina SYu (2015). Tropomyosin as a regulator of actin dynamics. In *International Review of Cell and Molecular Biology*, 255–291.
Li XE, Tobacman LS, Mun JiY, Craig Roger, Fischer S, Lehman W (2011). Tropomyosin position on F-actin revealed by EM reconstruction and computational chemistry. Biophys J 100, 1005–1013.
Meiring JCM, Bryce NS, Wang Y, Taft MH, Manstein DJ, Lau SL, Stear J, Hardeman EC, Gunning PW (2018). Co-polymers of actin and tropomyosin account for a major fraction of the human actin cytoskeleton. Curr Biol 28, 2331–2337.e5.
Monteiro PB, Lataro RC, Ferro JA, de Reinach FC (1994). Functional alpha-tropomyosin produced in *Escherichia coli*: a dipeptide extension can substitute the amino-terminal acetyl group. J Biol Chem 269, 10,461–10,466.
Moraczewska J, Nicholson-Flynn K, Hitchcock-DeGregori SE (1999). The ends of tropomyosin are major determinants of actin affinity and myosin subfragment 1-induced binding to f-actin in the open state. Biochemistry 38, 15,885–15,892.
Nicovich PR, Janco T, Sobey T, Gajwani M, Obeidy P, Whan R, Gaus K, Gunning PW, Coster CA, Böcking T (2016). Effect of Surface Chemistry on Tropomyosin Binding to Actin Filaments on Surfaces. Cytoskeleton 73, 729–738.
Nicovich PR, Walsh J, Böcking T, Gaus K (2017). NicoLase—an open-source diode laser combiner, fiber launch, and sequencing controller for fluorescence microscopy. PLoS One 12, e0173879.
Orzechowski M, Li XE, Fischer S, Lehman W (2014). An atomic model of the tropomyosin cable on f-actin. Biophys J 107, 694–699.
Palani S, Köster DV, Hatano T, Kamnev A, Kanamaru T, Brooker HR, Hernandez-Fernaud JR, Jones AME, Millar JBA, Mulvihill DP, Balasubramanian MK (2019). Phosphoregulation of Tropomyosin Is Crucial for Actin Cable Turnover and Division Site Placement. J Cell Biol 218, 3548–3559.
Pathan-Chhatbar S, Taft MH, Reindl T, Hundt N, Latham SL, Manstein DJ (2017). Three mammalian tropomyosin isoforms have different regulatory effects on nonmuscle myosin-2B and filamentous β-actinin vitro. J Biol Chem 293, 863–875.
Perry SV (2001). Vertebrate tropomyosin: distribution, properties and function. J Muscle Res Cell Motil 22, 5–49.
Pollard TD (2016). Actin and actin-binding proteins. Cold Spring Harb Perspect Biol 8, a018226.
Sao K, Jones TM, Doyle AD, Maity D, Schevzov G, Chen Y, Gunning PW, Petrie RJ (2019). Myosin II governs intracellular pressure and traction by distinct tropomyosin-dependent mechanisms. Mol Biol Cell 30, 1170–1181.
Schmidt WM, Lehman W, Moore JR (2015). Direct observation of tropomyosin binding to actin filaments. Cytoskeleton 72, 292–303.
Sckolnick M, Krementsova EB, Warshaw DM, Trybus KM (2016). Tropomyosin isoforms bias actin track selection by vertebrate myosin va. Mol Biol Cell 27, 2889–2897.
Shekhar S, Carlier M-F (2016). Single-filament kinetic studies provide novel insights into regulation of actin-based motility. Mol Biol Cell 27, 1–6.
Singh A, Hitchcock-DeGregori SE (2009). A Peek into tropomyosin binding and unfolding on the actin filament. PLoS One 4, e6336.
Tobacman LS (2008). Cooperative binding of tropomyosin to actin. Adv Exp Med Biol 644: 85–94.
Tojkander S, Gateva G, Schevzov G, Hotulainen P, Naumanen P, Martin C, Gunning PW, Lappalainen P (2011). A molecular pathway for myosin II recruitment to stress fibers. Curr Biol 21, 539–550.
Vilfan A (2001). The binding dynamics of tropomyosin on actin. Biophys J 81, 3146–3155.
Wegner A (1979). Equilibrium of the actin–tropomyosin interaction. J Mol Biol 131, 839–853.
Wegner A (1980). The interaction of alpha, alpha- and alpha, beta-tropomyosin with actin filaments. FEBS Lett 119, 245–248.
Wegner A, Ruhnau K (1988). Rate of binding of tropomyosin to actin filaments. Biochemistry 27, 6994–7000.
Wegner A, Walsh TP (1981). Interaction of tropomyosin–troponin with actin filaments. Biochemistry 20, 5633–5642.
Weigt C, Wegner A, Koch MH (1991). Rate and mechanism of the assembly of tropomyosin with actin filaments. Biochemistry 30, 10,700–10,707.
Wioland H, Guichard B, Senju Y, Myram S, Lappalainen P, Jégou A, Romet-Lemonne G (2017). ADF/Cofilin accelerates actin dynamics by severing filaments and promoting their depolymerization at both ends. Curr Biol 27, 1956–67.e7.
Wu J-Q, Kuhn JR, Kovar DR, Pollard TD (2003). Spatial and temporal pathway for assembly and constriction of the contractile ring in fission yeast cytokinesis. Dev Cell 5, 723–734.